IEEE Access
Multidisciplinary | Rapid Review | Open Access Journal

Received March 12, 2021, accepted April 28, 2021, date of publication May 7, 2021, date of current version May 17, 2021.

Digital Object Identifier 10.1109/ACCESS.2021.3078325

A Real-Time Cycle Slip Detection and Repair Method Based on Ionospheric Delay Prediction for Undifferenced Triple-Frequency BDS Signals

CHENXI ZHANG[1], YAMIN DANG[2], XIAOMING WANG[3], JINYI QUAN[4], AND ZHIGANG YU[1]

[1]School of Resources, Shandong University of Science and Technology, Tai'an 271019, China
[2]Institute of Geodesy and Geodynamics, Chinese Academy of Surveying and Mapping, Beijing 100830, China
[3]Aerospace Information Research Institute, Chinese Academy of Sciences, Beijing 100094, China
[4]Jinan Geotechnical Investigation and Surveying Institute, Jinan 250101, China

Corresponding author: Zhigang Yu (yuzhigangabc@163.com)

This work was supported in part by the China Natural Science Funds under Grant 41904033, in part by the Strategic Priority Research Program of the Chinese Academy of Sciences (CAS) under Grant XDA17010304, in part by the CAS Pioneer Hundred Talents Program, and in part by the Natural Science Foundation of Shandong Province under Grant ZR2019MD005.

ABSTRACT The detection and repair of cycle slips are key steps in high-accuracy GNSS (Global Navigation Satellite System) data processing using carrier phase observations. BDS (BeiDou Navigation Satellite System) triple-frequency observations provide better combinations for cycle slip detections and repairs compared to dual-frequency observations. Although a number of algorithms have been developed and may correctly detect cycle slips most of the time, the reliability of empirical thresholds methods cannot be guaranteed. In this study, an adaptive threshold is proposed for three sets of triple-frequency Geometry-Free (GF) pseudorange minus phase combinations to improve the cycle slip detection performance and reduce the false alarm rate of the cycle slip detection by combining the predicted epoch-differenced ionospheric delays under active ionospheric conditions. Moreover, in the cycle slip repair, the integral combined cycle slips are determined by directly rounding the estimated float-combined cycle slips, which will lead to a repair error if the between-epoch ionospheric variation is large. In this study, a new rounding method considering the predicted epoch-differenced ionospheric delays is proposed, and it is proven that the new method has a higher success rate for estimating the integer value of a cycle slip than the traditional method. The performance of the newly proposed method is validated by using static BDS triple-frequency observations that contain simulated cycle slips. BDS triple-frequency observations were collected at 30-s sampling intervals under active ionospheric conditions. The results show that this method can successfully detect and repair all slips of more than one cycle. In addition, dynamic BDS data collected with a vehicle-based receiver at a 1-s sampling intervals are processed, and the results show that the proposed method is also effective in the detection and repair of cycle slips in dynamic data.

INDEX TERMS BDS, triple-frequency, cycle slip, high ionospheric activity, adaptive threshold.

I. INTRODUCTION

To meet the needs of high-precision applications, the high-quality carrier phase measurements of GNSS must be utilized in data processing. However, inevitable cycle slips caused by a low signal-to-noise ratio, a failure of the receiver software or a strong ionospheric scintillation will greatly reduce the accuracy of the positioning results if the cycle slips are not correctly detected and repaired. Therefore, the correct detection and repair of cycle slips has become a very important step in high-accuracy data processing [1], [2].

Since the 1980s, cycle slip detection and repair algorithms have been proposed and studied for GNSS dual-frequency observations. For example, Gao and Li [3], Bisnath and Langley [4], and Chen *et al.* [5] proposed cycle-slip detection and repair methods by using the double-differences or triple-differences of dual-frequency observations. However, for these aforementioned cycle slip detection and repair

The associate editor coordinating the review of this manuscript and approving it for publication was Venkata Ratnam Devanaboyina.

methods, simultaneous observations collected from at least two receivers are required to form double-difference or triple-difference observations. Therefore, these methods are not suitable for cycle slip detections in precise point positioning (PPP), which only uses observations from a single receiver. The TurboEdit algorithm [6], which can be used in the PPP application, applies the Melbourne-Wübbena (MW) linear combination and Geometry-Free (GF) combination to detect cycle slips. Although this algorithm is one of the most commonly used dual-frequency and un-differenced cycle slip detection methods, it still has many deficiencies in many practical applications. First, the wavelengths of dual-frequency MW combinations are still relatively small, and this degrades the performance of the method when there is substantial pseudorange noise [7]. Second, MW combinations are not sensitive to two cycle slips with the same frequency. Furthermore, GF combinations could be inefficient in cases of active ionospheric conditions with large biases and quick variations [8]. Some improved methods have been proposed; e.g., Liu [9] employed the ionospheric total electron content rate (TECR) instead of the GF combination to implement dual-frequency cycle slip detection. However, this method is suitable only for data with a high sampling rate. Ju *et al.* [7] found many one-cycle slips in low-elevation BDS GEO carrier phase observations, and a combination of robust polynomial fitting algorithms and general autoregressive conditional heteroskedastic (GARCH) modeling techniques were employed to provide an adaptive detection threshold for GF combinations.

With the launch of a new generation of GNSS satellites, triple-frequency observations have become available; these observations allow the introduction of additional linear combinations (LC) with integer characteristics as well as less noise, longer wavelengths and weaker ionospheric delay than those associated with dual-frequency observations [10], [11]. In recent years, different algorithms have been proposed for triple-frequency cycle slip detections.

The triple-frequency LCs used for cycle slip detections include a GF combination and geometry-based (GB) combination. Dai *et al.* [12] proposed an instantaneous triple-frequency cycle slip detection and repair method that applies two GF phase combinations for detecting insensitive cycle slips and uses the least-squares ambiguity decorrelation adjustment (LAMBDA) algorithm to search for cycle slip candidates. Since only two geometry-free phase combinations are used in the method, some undetectable cycle slips remain [7]. Lacy *et al.* [13] proposed a cycle slip detection method by simultaneously adopting five GF combinations used in three cascading steps. However, the active ionospheric condition was not considered in this method, and the validation experiment was conducted only with 1Hz triple-frequency GPS data in a common multi-path observation environment. Banville and Langley [14] proposed a cycle slip detection method based on the GB model and discussed the sensitivity of this method to different ionospheric conditions. The main disadvantage of this method is its dependence on external information, such as precise satellite orbit and clock deviations. Li *et al.* [8] further proposed a new GB ionosphere-weighted (GBIW) model dedicated to efficiently estimating cycle slips in data collected under active ionospheric conditions containing a gap.

The performance of a cycle slip detection method can be affected by ionospheric conditions and large sampling intervals or even data gaps. The use of a second-order time-difference algorithm is helpful for mitigating the impacts of between-epoch ionospheric residuals on cycle slip detections (Cai *et al.* [15], Liu *et al.* [16]). However, these algorithms enlarge the pseudorange noise. For regions in which the ionosphere varies smoothly, this method easily misses cycle slips, and its applicability is thus limited. Geometry-free and ionosphere-free (GFIF) combinations have been used in many studies to detect and repair cycle slips by eliminating geometric and ionospheric terms (Huang *et al.* [17]), but the detection success rate of this method decreases when high pseudorange noise is present.

There have been some studies on modeling and forecasting ionospheric delays [7], [18]–[20], making it is possible to incorporate an ionosphere forecasting model in cycle slip detections and repairs. Zhao *et al.* [21] sequentially determined cycle slips on the extra-wide lane (EWL), wide lane (WL), and narrow lane (NL) in three cascading steps. This method compensates for an ionospheric delay by using ionospheric predictions, and it is suitable for the real-time detection and repair of cycle slips under low rates or active ionospheric conditions. To repair triple-frequency cycle slips, Chang *et al.* [22] proposed an adaptive Kalman filter based on variance component estimations to predict ionospheric delays. These methods consider high ionospheric activity, but studies on triple-frequency cycle slips under high noise levels are relatively few, especially regarding detection combinations that are based on pseudorange observations.

Although these algorithms may correctly detect cycle slips most of the time, the reliability of these cycle slip detection and repair methods cannot be guaranteed. The empirical thresholds, which are used to decide whether a cycle slip occurs, may be too tolerant or too strict for cycle slip detections. Deng *et al.* [23] proposed an algorithm for reliably detecting and repairing cycle slips using three GF triple-frequency combinations and dynamically determined thresholds without considering ionosphere disturbances.

According to the above discussion, a real-time cycle slip detection and repair method has been proposed for BDS triple-frequency between-epoch differenced observations that have low sampling rates, large noise and are collected under active ionospheric conditions. An adaptive threshold determination method developed by considering an active ionospheric condition is proposed, and three linearly independent GF pseudorange minus phase combinations are used jointly to reduce the false rate and miss rate of the cycle slip detections. To take into account the time-varying characteristics of the ionospheric delay variation, a moving window strategy is adopted, namely, only recent data are used to construct the

model that is used at the current epoch. The relationships among the rounding success rate, the ionospheric variation and the combined noise are analyzed to propose an optimal strategy for accurately estimating the integer values of cycle slips while considering the predicted epoch-differenced ionospheric delay.

In Sect. 2, the cycle slip detection and repair method designed based on GF triple-frequency pseudorange minus phase combinations is presented. In Sect. 3, an adaptive threshold algorithm based on polynomial fitting is constructed. In Sect. 4, the cycle slip repair method and the strategy used for the estimations of the integer values of cycle slips are given. In Sect. 5, the performance of the proposed method is validated using real BDS data. The discussion and conclusion are presented in Sect. 6.

II. METHOD OF TRIPLE-FREQUENCY CYCLE SLIP DETECTION

Without a loss of generality, the nondispersive terms, including the geometric range, orbit errors, clock errors, and tropospheric delays, are lumped together and simply denoted as the geometric range. The slowly varying items, e.g., the hardware delay, are ignored since they will be significantly reduced in the epoch-differenced observations. The residuals of the multipath errors after the epoch difference is applied are regarded as completely random noise. The pseudorange and carrier phase observation equations are expressed as follows:

$$P_i = \rho + \eta_i I_1 + \varepsilon_{P_i} \tag{1}$$

$$\lambda_i \varphi_i = \rho - \eta_i I_1 + \lambda_i N_i + \lambda_i \varepsilon_{\varphi_i} \tag{2}$$

The mathematical notation in this section is summarized in Table 1.

According to the triple-frequency observation theories [24], let α, β, γ (integers) and $a, b, c (a + b + c = 1)$ denote the LC coefficients of the phase and pseudorange observations, respectively. We then have the following LC observation equations:

$$P_{abc} = \rho + \eta_{abc} I_1 + \varepsilon_{P_{abc}} \tag{3}$$

$$\lambda_{\alpha\beta\gamma} \varphi_{\alpha\beta\gamma} = \rho - \eta_{\alpha\beta\gamma} I_1 + \lambda_{\alpha\beta\gamma} N_{\alpha\beta\gamma} + \lambda_{\alpha\beta\gamma} \varepsilon_{\varphi_{\alpha\beta\gamma}} \tag{4}$$

The triple-frequency GF pseudorange minus phase combination can be expressed as follows:

$$l_{\alpha\beta\gamma,abc} = \varphi_{\alpha\beta\gamma} - P_{abc}/\lambda_{\alpha\beta\gamma} = N_{\alpha\beta\gamma} - \varsigma I_1 + e_{\alpha\beta\gamma,abc} \tag{5}$$

where $\varsigma = (\eta_{abc} + \eta_{\alpha\beta\gamma})/\lambda_{\alpha\beta\gamma}$ and $e_{\alpha\beta\gamma,abc} = \varepsilon_{\varphi_{\alpha\beta\gamma}} - \varepsilon_{P_{abc}}/\lambda_{\alpha\beta\gamma}$. The differences in the observations between adjacent epochs are constructed to detect and repair the cycle slips. We now have the following equation (in cycles):

$$\begin{aligned} \Delta l_{\alpha\beta\gamma,abc} &= \Delta\varphi_{\alpha\beta\gamma} - \Delta P_{abc}/\lambda_{\alpha\beta\gamma} \\ &= \Delta N_{\alpha\beta\gamma} - \varsigma \Delta I_1 + \Delta e_{\alpha\beta\gamma,abc} \end{aligned} \tag{6}$$

When the ionospheric delay varies smoothly, the epoch-differenced ionospheric delay terms in formula (6) are always ignored.

TABLE 1. Mathematic notation.

i	Three frequencies, $i = 1, 2, 3$
P_i	The pseudorange observations (in meters)
φ_i	The carrier phase observations (in cycles)
ρ	The (lumped) geometric range
f_i , λ_i	The frequency and wavelength (in meters)
I_1	The first-order ionospheric delay on f_1 (in meters)
N_i	The integer ambiguity
η_i	The ionospheric delay coefficient with respect to the ionospheric delay on f_1, $\eta_i = f_1^2 / f_i^2$
ε_{R_i}	The pseudorange noise (in meters)
ε_{φ_i}	The carrier phase observation noise (in cycles)
P_{abc}	LC pseudorange observations, $P_{abc} = aP_1 + bP_2 + cP_3$
$\varphi_{\alpha\beta\gamma}$	LC carrier phase observations, $\varphi_{\alpha\beta\gamma} = \alpha\varphi_1 + \beta\varphi_2 + \gamma\varphi_3$
$\lambda_{\alpha\beta\gamma}$	LC wavelength, $\lambda_{\alpha\beta\gamma} = c/(\alpha f_1 + \beta f_2 + \gamma f_3)$
$N_{\alpha\beta\gamma}$	LC integer ambiguity, $N_{\alpha\beta\gamma} = \alpha N_1 + \beta N_2 + \gamma N_3$
η_{abc} , $\eta_{\alpha\beta\gamma}$	The first-order ionospheric delay coefficients of the LC pseudorange and phase observations, $\eta_{abc} = a\eta_1 + b\eta_2 + c\eta_3$, $\eta_{\alpha\beta\gamma} = (\alpha f_1\eta_1 + \beta f_2\eta_2 + \gamma f_3\eta_3) / (\alpha f_1 + \beta f_2 + \gamma f_3)$
$\varepsilon_{P_{abc}}$, $\varepsilon_{\varphi_{\alpha\beta\gamma}}$	The LC pseudorange and phase noise, $\varepsilon_{P_{abc}} = a\varepsilon_{P_1} + b\varepsilon_{P_2} + c\varepsilon_{P_3}$, $\varepsilon_{\varphi_{\alpha\beta\gamma}} = \alpha\varepsilon_{\varphi_1} + \beta\varepsilon_{\varphi_2} + \gamma\varepsilon_{\varphi_3}$
$l_{\alpha\beta\gamma,abc}$	The triple-frequency GF pseudorange minus phase combination
Δ	The epoch-difference
$\sigma_{N_{\alpha\beta\gamma}}$	The standard deviations (STDs) of $N_{\alpha\beta\gamma}$
$\sigma_{\Delta N_{\alpha\beta\gamma}}$	The standard deviations (STDs) of $\Delta N_{\alpha\beta\gamma}$

It is assumed that the noise terms of the carrier phase observations in each frequency are independent in time and are identical in variance, i.e., $\sigma_{\varphi_1} = \sigma_{\varphi_2} = \sigma_{\varphi_3} = \sigma_\varphi$; it is assumed that the same is true for the pseudorange noise terms, i.e., $\sigma_{P_1} = \sigma_{P_2} = \sigma_{P_3} = \sigma_P$. The standard deviations (STDs) of $\Delta N_{\alpha\beta\gamma}$ are expressed by the following equation.

$$\begin{aligned} &\sigma_{\Delta N_{\alpha\beta\gamma}} \\ &= \sqrt{2}\sigma_{N_{\alpha\beta\gamma}} \\ &= \sqrt{2} \cdot \sqrt{(\alpha^2 + \beta^2 + \gamma^2)\sigma_\varphi^2 + (a^2 + b^2 + c^2)\sigma_P^2/\lambda_{\alpha\beta\gamma}^2} \end{aligned} \tag{7}$$

When the following condition is satisfied, a cycle slip can be detected:

$$\left|\Delta l_{\alpha\beta\gamma,abc}\right| > \kappa \cdot \sigma_{\Delta N_{\alpha\beta\gamma}} \tag{8}$$

where $\kappa \cdot \sigma_{\Delta N_{\alpha\beta\gamma}}$ is the critical value for the cycle slip detection criterion and the scalar κ denotes the multiple of the standard deviation; $\kappa = 3$ denotes a 99.7% confidence level [25]. The smaller the STD of $\Delta N_{\alpha\beta\gamma}$ is, the higher the cycle slip rounding success rate is [26].

Pseudorange noise is the main factor affecting the accuracy of the cycle slip detection. According to formula (7), to minimize the STD of the GF combination, the coefficient

TABLE 2. Some typical combinations.

Combination Coefficient	$\lambda_{\alpha\beta\gamma}$ /m	$\eta'_{\alpha\beta\gamma}$	$\sigma_{N_{\alpha\beta\gamma}}$ /cycle		
			$\sigma_P = 0.3m$	$\sigma_P = 0.6m$	$\sigma_P = 3m$
(4, -2, -3) ※	12.21	-11.75	0.056	0.061	0.152
(0, -1,1)	4.88	-0.04	0.038	0.072	0.355
(-4,1,4) ※	8.14	11.71	0.061	0.072	0.220
(-3,6, -2)※	13.32	12.071	0.071	0.075	0.148
(-1, -5,6)	20.93	-0.362	0.079	0.081	0.114
(7,-8,1)	146.53	-23.82	0.107	0.107	0.107
(5,3, -9)	29.31	-11.39	0.107	0.108	0.122

of the pseudorange combination is set to 1/3. To select the optimal GF pseudorange minus phase combinations, four conditions are required for the carrier phase combination measurement [4]: The combination coefficients must be integers; the wavelength must be long; the ionospheric delay coefficient must be small; and the combined noise in the cycles must be small. Assuming that the STD of the phase observations is $\sigma_\varphi = 0.01cycle$, the STD of the pseudorange observations is $\sigma_P = 0.3m, 0.6m, 3m$. As suggested by [16], to reduce the search scope of the optimal combination, the combined wavelength should be larger than 4m, and the sum of combination coefficient should be smaller than 2. With these two criteria, we can find some suitable coefficients in the range of $[-10, 10]$. Table 2 shows the combined wavelengths ($\lambda_{\alpha\beta\gamma}$), ionospheric coefficients in cycles ($\eta'_{\alpha\beta\gamma} = \eta_{\alpha\beta\gamma}/\lambda_{\alpha\beta\gamma}$) and STDs ($\sigma_{N_{\alpha\beta\gamma}}$) of the first six optimal triple-frequency combinations.

It can be seen in Table 2 that STD of the combined ambiguity of BDS triple-frequency combinations (0, −1,1), (4, −2, −3), (−4,1,4) and (−3,6, −2) is small, but the ionospheric coefficient of the last combination is large. Although the ionospheric coefficient of the dual-frequency combination (0, −1,1) is small, the STD of the combined noise is large with the increase in pseudorange noise, so this combination is abandoned. Considering the uncorrelated conditions, three combinations of superscript "※" are selected: (−4,1,4), (−3,6, −2) and (4, −2, −3). Since many works have studied the characteristics of different combinations of triple-frequency signals, such as [27], these characteristics will not be analyzed in detail here.

In this paper, we assumed that the noises of all codes are the same. Based on this assumption, we let a = b = c = 1/3 to minimize the impact of the pseudorange noise. However, as suggested by previous studies and our experiment results shown in Figure 1, the noise of B3 is lower than those of the other BDS pseudorange measurements. Therefore, it is reasonable to set a different STD for the B3 code from those of the other BDS codes.

According to the statistics of the RMSs of the pseudorange noises (as suggested by Figure 1), the pseudorange noises of

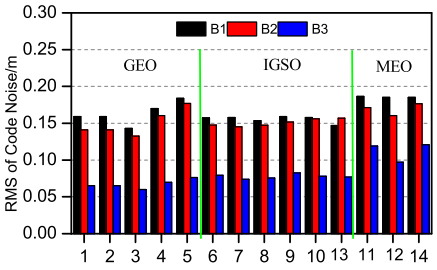

FIGURE 1. The RMSs of pseudorange noises.

B1 and B2 are similar, while the code noise of B3 is about half those of B1 and B2; thus, we set $\sigma_{P_1} = \sigma_{P_2}, \sigma_{P_3} = 0.5\sigma_{P_1}$. Based on this assumption, we let a = b = 1/4 and c = 1/2 to calculate the STDs of the $N_{\alpha\beta\gamma}$ values of the selected combinations (−4, 1, 4), (−3, 6, −2) and (4, −2, −3). The results indicate that the STDs of $N_{\alpha\beta\gamma}$ are almost the same as those shown in the results in Table 2. So, assuming the noises of B1, B2 and B3 are the same will not affect the cycle slip detection. In addition, the code coefficient (1/3,1/3,1/3) was also recommended in [16] and [23] and it is also suitable for GPS.

In the classical algorithms of GF triple-frequency pseudorange minus phase combinations, as mentioned above, it is generally assumed that the ionospheric delay varies smoothly, and the ionospheric delay terms are thus ignored [28]. Actually, the residual ionospheric variation remains in the first-order epoch-difference of $N_{\alpha\beta\gamma}$, especially in the active ionospheric condition, indicating that the $\varsigma\Delta I_1$ term cannot be ignored. When the ionosphere is active, the epoch-differenced ionospheric delay still shows systematic variations instead of random noise. In that case, the second-order or third-order polynomial can be applied to predict the epoch-differenced ionospheric delay [29].

III. CONSTRUCTION OF AN ADAPTIVE THRESHOLD

From formula (6), it can be determined that $\Delta l_{\alpha\beta\gamma,abc}$ includes the epoch-differenced ionospheric delay, ambiguity and combination noises. With a change in the surrounding environment, mainly in the ionospheric delay or observation noise, the adaptability of the empirical threshold is poor, reducing the performance of the cycle slip detection. To adapt to these changes, we propose to construct an adaptive threshold instead of an empirical threshold.

Since the polynomial regression model is widely used to express variation in a variable, a polynomial regression function of time is introduced to fit the time series of each cycle slip detection combination $\Delta l_{\alpha\beta\gamma}$ (omitting the pseudorange observation coefficient) to describe the epoch-differenced ionospheric delay. The commonly used p-order polynomial function is as follows:

$$y_j = \mu_0 + \mu_1(t_j - t_0) + \cdots + \mu_p(t_j - t_0)^p + \varepsilon_j \qquad (9)$$

where j represents epoch n, such that $j = 1,2,\ldots\ldots n$; y_j is the cycle slip detection combination $\Delta l_{\alpha\beta\gamma}$ in formula (6);

t_j represents the instantaneous time of the observation sample; $\mu_1, \cdots, \mu_p$ represents the unknown polynomial coefficient; and ε_j represents the overall noise of the cycle slip detection combination. The order of p should reflect the change in the combination of each cycle with time in the given data period. For example, when the ionosphere changes slowly between the epochs, the deviation portion of the cycle slip combination remains constant, i.e., at $p = 0$.

To continue the estimation and analysis, the following symbols are introduced.

$$\mathbf{H}_i = \begin{pmatrix} 1 & t_1 - t_0 & (t_1 - t_0)^2 & \cdots & (t_1 - t_0)^{p_i} \\ 1 & t_2 - t_0 & (t_2 - t_0)^2 & \cdots & (t_2 - t_0)^{p_i} \\ \vdots & \vdots & \vdots & \ddots & \vdots \\ 1 & t_j - t_0 & (t_j - t_0)^2 & \cdots & (t_j - t_0)^{p_i} \end{pmatrix}_{n \times p_i}$$

$$\mathbf{Y}_i = \begin{pmatrix} \Delta l_{\alpha_i\beta_i\gamma_i,1} \\ \Delta l_{\alpha_i\beta_i\gamma_i,2} \\ \vdots \\ \Delta l_{\alpha_i\beta_i\gamma_i,n} \end{pmatrix}_{n \times 1}, \quad \mu_i = \begin{pmatrix} \mu_{i,1} \\ \mu_{i,2} \\ \vdots \\ \mu_{i,p_i} \end{pmatrix}_{p_i \times 1},$$

$$\varepsilon_{\mathbf{Y}_i} = \begin{pmatrix} \varepsilon_{i,1} \\ \varepsilon_{i,2} \\ \vdots \\ \varepsilon_{i,n} \end{pmatrix}_{n \times 1}$$

For the three $\Delta l_{\alpha\beta\gamma}$ values, the polynomial regression model can be abbreviated as follows:

$$\mathbf{Y}_i = \mathbf{H}_i \mu_i + \varepsilon_{\mathbf{Y}_i} \tag{10}$$

where i represents three GF cycle slip detection combinations, such that i = 1,2,3, including (−4, 1, 4), (−3, 6, −2), and (4, −2, −3); p_i is the fitting order of the i th slip detection combination, generally shown as $p_1 = p_2 = p_3 = p$; $\varepsilon_{\mathbf{Y}_i}$ is the total noise item of the ith slip detection combination, such that $E(\varepsilon_{\mathbf{Y}_i}) = 0$; and it can be validated that $Cov(\varepsilon_{\mathbf{Y}_i}) = \sigma^2_{\mathbf{Y}_i}\mathbf{I}_n$, $\mathbf{I}_n$ is an n-dimensional unit matrix.

The fitting coefficients and residual vectors obtained from the ordinary least squares are expressed as follows.

$$\hat{\boldsymbol{\mu}}_i = (\mathbf{H}_i^T \mathbf{H}_i)^{-1} \mathbf{H}_i^T \mathbf{Y}_i \tag{11}$$

$$\mathbf{V}_i = (\mathbf{I}_n - \mathbf{H}_i(\mathbf{H}_i^T \mathbf{H}_i)^{-1} \mathbf{H}_i^T)\mathbf{Y}_i \tag{12}$$

The STD of the residual statistics is described by the following formula.

$$\sigma = \sqrt{\mathbf{V}_i^T \mathbf{V}_i / (n - p - 1)} \tag{13}$$

For most cases, the sample size n is generally large enough, e.g., from tens to hundreds, depending on the sampling interval and data period. The p value is usually quite small and plays a very small role in the standard deviation calculation. As widely accepted, the p value is usually set to $p_1 = p_2 = p_3 = 2$ [20].

Because the correlation between observations decrease with time, a sliding window with a length of m is adopted in the calculation of the STD residuals. As suggested by [8], for data with a 30-s interval, the window size is set to 10 epochs. For data with a 1-s interval, 50 epochs are taken as the window size based on experimental results. The adaptive threshold is built as follows.

First, the polynomial model of the window with m samples is used to predict the ionospheric delay epoch difference of epoch $m + 1$ by the following formula.

$$\bar{y}_{i,m+1} = \mu_0 + \mu_1(t_{m+1} - t_0) + \cdots + \mu_p(t_{m+1} - t_0)^p \tag{14}$$

Then, the STD of the residuals of m sample windows is taken as the STD of the next epoch estimation, which can be expressed as follows:

$$\hat{\sigma}(m+1) = \sqrt{\mathbf{V}_i^T(m)\mathbf{V}_i(m)/(m - p - 1)} \tag{15}$$

where $\mathbf{V}_i(m)$ is the residual matrix of $m \times 1$, which is calculated as in formula (13), but m samples are used.

The $(m+1)$-epoch adaptive threshold model of the ith cycle slip detection combination is constructed as the predicted value of the epoch-differenced ionospheric delay plus the κ- fold STD estimation, that is, as described below.

$$\left|\Delta l_{\alpha_i\beta_i\gamma_i}\right| > \bar{y}_{i,m+1} \pm \kappa \cdot \hat{\sigma}(m+1) \tag{16}$$

Taking $\kappa = 3$, the equation above corresponds to a 99.7% confidence level. When the above formula is satisfied, it shows that there is a combined cycle slip in the given epoch.

For the beginning of periods of several epochs, it should be assured that cycle slips are absent in order to estimate the ionospheric delay to a satisfactory accuracy. A quality check procedure is conducted to select data with a good quality for estimations with the ionospheric delay model. Taking data with a 30-s sampling interval as an example, the quality check steps are: (1) Fit the epoch-differenced ionospheric delays at the first 10 observations with a polynomial model, represented as $\bar{y}_{i,m}$(m = 1,2,..., 10); (2) Calculate the STD of the residual statistics, $\hat{\sigma}_0$, according to formula (13); (3) Construct the cycle slip detection threshold of these 10 epochs as $\bar{y}_{i,m} \pm \kappa \cdot \hat{\sigma}_0$ and detect whether there is a cycle slip present in these 10 observations with the threshold; (4) If there is no cycle slip detected, these observations are then regarded as having good quality and used for the building of the ionospheric delay model; (5) If there is a cycle slip detected, this quality check procedure is then repeated and applied to the next 10 observations to search for 10-epoch data with good quality.

IV. ROUNDING STRATEGY FOR CYCLE SLIP REPAIR

Once a cycle slip is successfully detected, determining its values exactly still presents a significant challenge [30]. Assuming the cycle slips on three separate frequencies are $\Delta N_1, \Delta N_2, \Delta N_3$, if a cycle slip occurs in a certain epoch, the corresponding three-cycle slip detection combinations are $\Delta N_{\alpha_1\beta_1\gamma_1}, \Delta N_{\alpha_2\beta_2\gamma_2}, \Delta N_{\alpha_3\beta_3\gamma_3}$, respectively. The relationships between the cycle slip detection combinations and the original cycle slips of each frequency can be defined as

follows.

$$\begin{bmatrix} \alpha_1 & \beta_1 & \gamma_1 \\ \alpha_2 & \beta_2 & \gamma_2 \\ \alpha_3 & \beta_3 & \gamma_3 \end{bmatrix} \begin{bmatrix} \Delta N_1 \\ \Delta N_2 \\ \Delta N_3 \end{bmatrix} = \begin{bmatrix} \Delta N_{\alpha_1\beta_1\gamma_1} \\ \Delta N_{\alpha_2\beta_2\gamma_2} \\ \Delta N_{\alpha_3\beta_3\gamma_3} \end{bmatrix} \quad (17)$$

With a sufficiently high accuracy, the float estimate of the combined integer ambiguity can be simply rounded to obtain the integer estimate of the cycle slip with a sufficiently high success rate. However, when the ionosphere is active or when the pseudorange noise is high, this method becomes unreliable and inaccurate. The following discussion is about the success rate of rounding the estimated float-combined cycle slip.

The rounding success rate is introduced to evaluate the performance of the cycle slip detection. Assume that $\Delta N_{\alpha\beta\gamma}$ has a normal distribution, as follows:

$$\Delta\hat{N}_{\alpha\beta\gamma} \sim (\Delta N_{\alpha\beta\gamma}, \sigma^2_{\Delta\hat{N}_{\alpha\beta\gamma}}) \quad (18)$$

where $\Delta N_{\alpha\beta\gamma}$ is the actual epoch-differenced ambiguity. Suppose $\Delta\breve{N}_{\alpha\beta\gamma}$ is the integer that is the closest to $\Delta\hat{N}_{\alpha\beta\gamma}$.

$$\Delta\breve{N}_{\alpha\beta\gamma} = \text{int}(\Delta\hat{N}_{\alpha\beta\gamma}) \quad (19)$$

The probability that $\Delta\breve{N}_{\alpha\beta\gamma}$ takes the integer q can be expressed as follows [26].

$$P(\Delta\breve{N}_{\alpha\beta\gamma} = q) = \int_{i-\Delta N_{\alpha\beta\gamma}}^{i-\Delta N_{\alpha\beta\gamma}} (1/\sqrt{2\pi}\sigma_{\Delta\hat{N}_{\alpha\beta\gamma}}) \cdot \exp(-0.5z^2/\sigma^2_{\Delta\hat{N}_{\alpha\beta\gamma}})dz \quad (20)$$

Based on this formula, the probability of correctly repairing cycle slip $\Delta N_{\alpha\beta\gamma}$ can be obtained by rounding the estimated float-combined cycle slip $\Delta\hat{N}_{\alpha\beta\gamma}$, which can be calculated by the following formula:

$$\begin{aligned} P(\Delta\breve{N}_{\alpha\beta\gamma} = \Delta N_{\alpha\beta\gamma}) &= P(\left|\Delta\hat{N}_{\alpha\beta\gamma} - \Delta N_{\alpha\beta\gamma}\right| \le 0.5) \\ &= 2\Phi(0.5\sigma^{-1}_{\Delta\hat{N}_{\alpha\beta\gamma}}) - 1 \end{aligned} \quad (21)$$

where $\Phi(x) = \int_{-\infty}^{x} (1/\sqrt{2\pi}) \cdot \exp(-0.5z^2)dz$. It can be seen from formula (21) that the different $\sigma_{\Delta\hat{N}_{\alpha\beta\gamma}}$(STD of $\Delta\hat{N}_{\alpha\beta\gamma}$) values correspond to different rounding success rates. With a decrease in $\sigma_{\Delta\hat{N}_{\alpha\beta\gamma}}$, the probability of obtaining the correct cycle slip $\Delta N_{\alpha\beta\gamma}$ by rounding increases.

Taking ionospheric variations into account, the rounding success rate can be expressed as follows [31]:

$$P_{bias} = \Phi((1 + 2bias_{ion})/2\sigma_{\Delta\hat{N}_{\alpha\beta\gamma}}) + \Phi((1 - 2bias_{ion})/2\sigma_{\Delta\hat{N}_{\alpha\beta\gamma}}) - 1 \quad (22)$$

where $bias_{ion} = -\varsigma\Delta I_1$. Figure 2(a) shows the relationships among the variation in the STD($\sigma_{\Delta\hat{N}_{\alpha\beta\gamma}}$), the epoch-differenced ionospheric delay (ΔI_1) and the rounding success rate. Figure 2(b) shows the relationship between ΔI_1 and $\sigma_{\Delta\hat{N}_{\alpha\beta\gamma}}$ when the rounding success rate (SR) exceeds 99.99%.

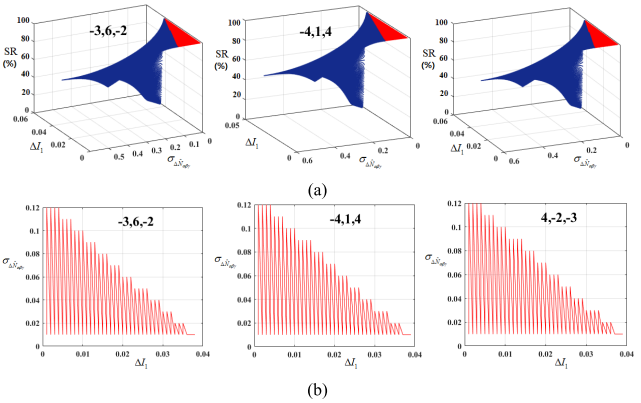

FIGURE 2. Relationships among the rounding success rate(SR), ΔI_1, and $\sigma_{\Delta\hat{N}_{\alpha\beta\gamma}}$.

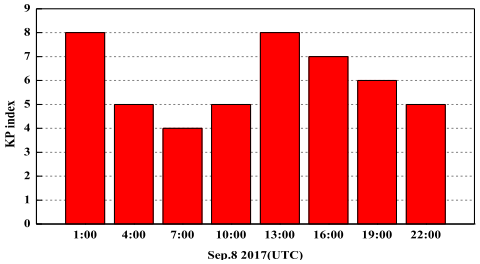

FIGURE 3. Geomagnetic Kp index on Sep. 8, 2017.

In Figure 2(a), the red area indicates that the rounding success rate is greater than or equal to 99.99%. In the blue area, the rounding success rate is less than 99.99%. It can be seen that the success rate changes with variations in the epoch-differenced ionospheric delay and the standard deviation of the noise. It can be seen in Figure 2(b) that to obtain a rounding success rate greater than 99.99%, the maximum $\sigma_{\Delta\hat{N}_{\alpha\beta\gamma}}$ can be taken as 0.12 *cycles* when ΔI_1 is as small as $0.001m$, and the maximum ΔI_1 can be taken as $0.37m$ when $\sigma_{\Delta\hat{N}_{\alpha\beta\gamma}}$ is as small as 0.01 *cycles*. It can be shown that when $\sigma_{\Delta\hat{N}_{\alpha\beta\gamma}}$ and ΔI_1 exceed 0.12 *cycles* and $0.37m$, respectively, the success rate will start to be less than 99.99%. In an actual observation environment, the noise and ionospheric variation are complex, so the situation is not sufficiently accurate for the use of direct rounding. Especially in the active ionospheric condition or when the pseudorange noise is large, the direct rounding method affects the accurate repair of cycle slips. Therefore, it is proposed that the prediction term of the epoch-differenced ionospheric delay be removed in the GF combination before it is rounded to an integer. It is assumed that a cycle slip is detected in the $(m + 1)$th epoch and is rounded according to the following rounding strategy.

$$\Delta\breve{N}_{\alpha_i\beta_i\gamma_i}(m+1) = \text{int}[\Delta\hat{N}_{\alpha_i\beta_i\gamma_i}(m+1) - \bar{y}_{i,m+1}] \quad (23)$$

The estimated STD of each GF combination is used to calculate the rounding success rate of the updated epoch. The

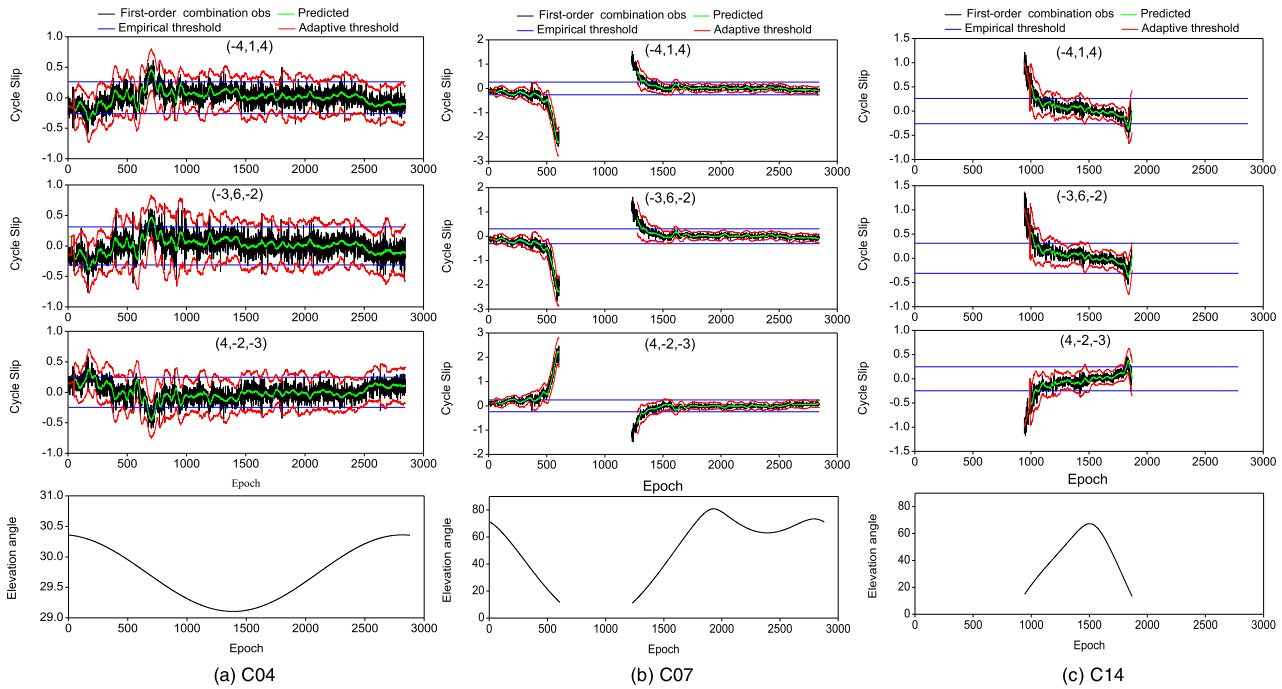

FIGURE 4. Comparison of detection results between the empirical threshold (blue) and adaptive threshold (red) for C04, C07, and C14 (Obs1).

expression is shown below.

$$P_{m+1}(\Delta\check{N}_{\alpha_i\beta_i\gamma_i} = \Delta N_{\alpha_i\beta_i\gamma_i}) = 2\Phi(0.5\hat{\sigma}^{-1}(m+1)) - 1 \tag{24}$$

When the ionosphere is active or the pseudorange noise is large, the model can capture the change in the rounding success rate sensitively. If the rounding success rate is high, the cycle slip value of each frequency point can be calculated directly after rounding. With an increase in noise level, the rounding success rate decreases continuously. The LAMBDA algorithm can then be used to search for the correct cycle slip.

V. DATA TESTS AND ANALYSIS

For the convenience of description, the GF pseudorange minus phase combination cycle slip detection and repair method designed using the empirical threshold and direct rounding of the cycle slip estimate is called the Empirical Threshold (ET) method, and the proposed cycle slip detection and repair method designed using an adaptive threshold and rounding of the cycle slip estimate while considering the predicted epoch-differenced ionospheric delay is called the Adaptive Threshold (AT) method.

A. EXPERIMENT WITH STATIC OBSERVATIONS

The experiment was conducted on Sep. 8, 2017, when there was a severe magnetic storm. Figure 3 shows the geomagnetic Kp index on Sep. 8, 2017 (http://www.sepc.ac. cn). The average Kp index is 6, which also indicates that the level of ionospheric activity was high [15].

The station JFNG is located in Jiufeng, China, where a significant change of TEC was experienced during our experimental period. The triple-frequency data of BDS C02 (GEO), C07 (IGSO) and C14 (MEO) observed by TRIMBLE NETR9 were analyzed at this station. The sampling interval was 30s. Figure 4 displays the between-epoch, first-order triple-frequency pseudorange minus phase combination for the raw observations without cycle slips and with low noises (Obs1). In Figure 4, the blue lines denote the empirical threshold, and the red lines denote the adaptive threshold. The green lines indicate the epoch-differenced ionospheric delay forecast values.

To investigate the performance of the methods in the detecting and repairing cycle slips in observations with high noise, a new observation (Obs2) set was simulated by adding noise into the raw observations, making the STD of the new noise set to be 3 m. Both the Adaptive Threshold Method and Empirical Threshold Method have been used to detect cycle slips in these simulated observations. Figure 5 displays the between-epoch, first-order triple-frequency pseudorange minus phase combination without cycle slips for the observations with high noise (Obs2).

It can be seen in Figures 4-5 that the three cycle slip combinations change rapidly with time due to the rapid change of the ionosphere, especially at low elevations. In this case, the changes would result in a large number of false alarms if the empirical threshold were directly used without any adjustment. However, the adaptive threshold calculated with AT method can accurately capture the rapid change in the ionosphere and thus determine an optimal threshold value, greatly reducing the cycle slip false alarm rate.

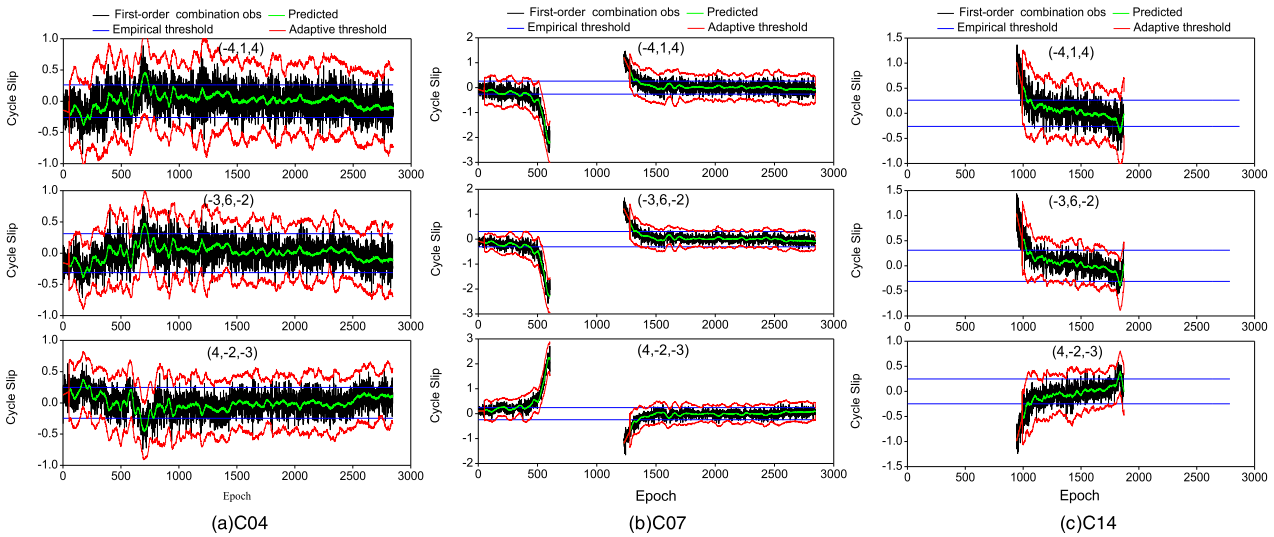

FIGURE 5. Comparison of detection results between the empirical threshold (blue) and adaptive threshold (red) for C04, C07, and C14 (Obs2).

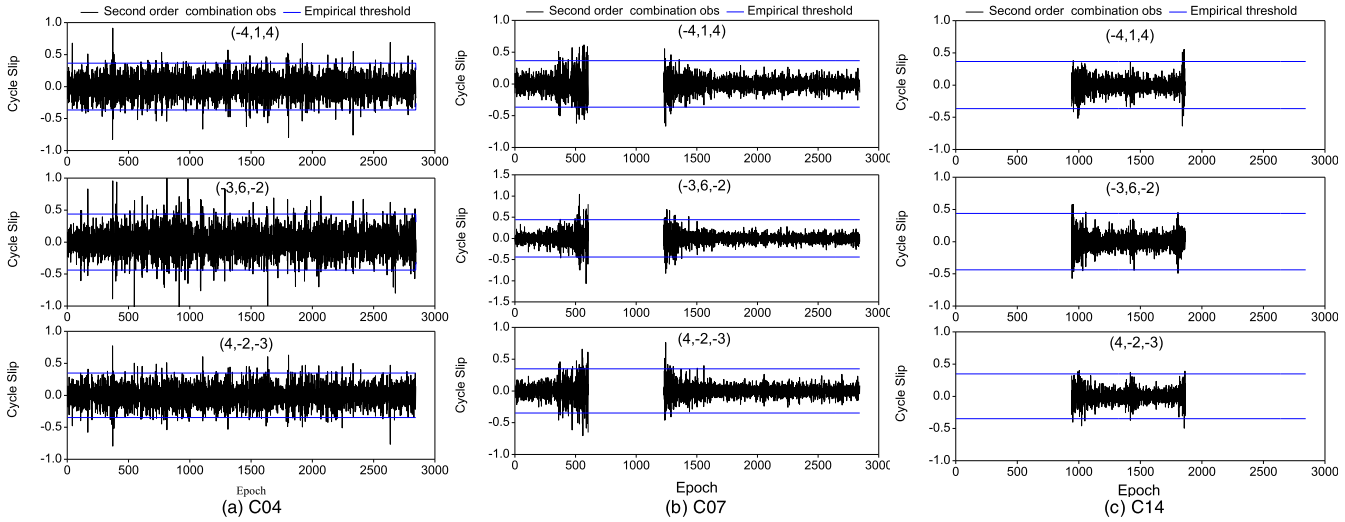

FIGURE 6. Second-order time-difference combination without cycle slips for C04, C07, and C14 (Obs1).

TABLE 3. Comparison of false alarms among the empirical threshold(ET), adaptive threshold(AT) and STPIR methods.

PRN	Total epochs	Data type	-4,1,4			-3,6,-2			4,-2,-3		
			ET	AT	STPIR	ET	AT	STPIR	ET	AT	STPIR
C04	2846	Obs1	232	29	107	201	43	128	264	33	103
		Obs2	724	12	860	329	30	329	525	17	516
C07	2231	Obs1	349	22	46	281	26	46	372	20	45
		Obs2	650	10	567	341	13	122	492	16	301
C14	930	Obs1	103	5	11	64	7	9	106	7	9
		Obs2	243	7	245	94	10	51	165	10	128

According to [15], the use of a second-order, time-differenced phase ionospheric residual (STPIR) method will mitigate the impact of between-epoch ionospheric variations and can improve the rounding success rate of estimated float cycle slips under high ionospheric activity conditions. To compare the performances of the STPIR algorithm and the newly proposed methods for cycle slip detections, the STPIR method is adopted in this study to detect cycle slips using formulas (25) and (26), as suggested by [15], [16].

$$\nabla\Delta l_{\alpha\beta\gamma,abc} = \Delta l_{\alpha\beta\gamma,abc}(t)\text{-}\Delta l_{\alpha\beta\gamma,abc}(t-1) \qquad (25)$$

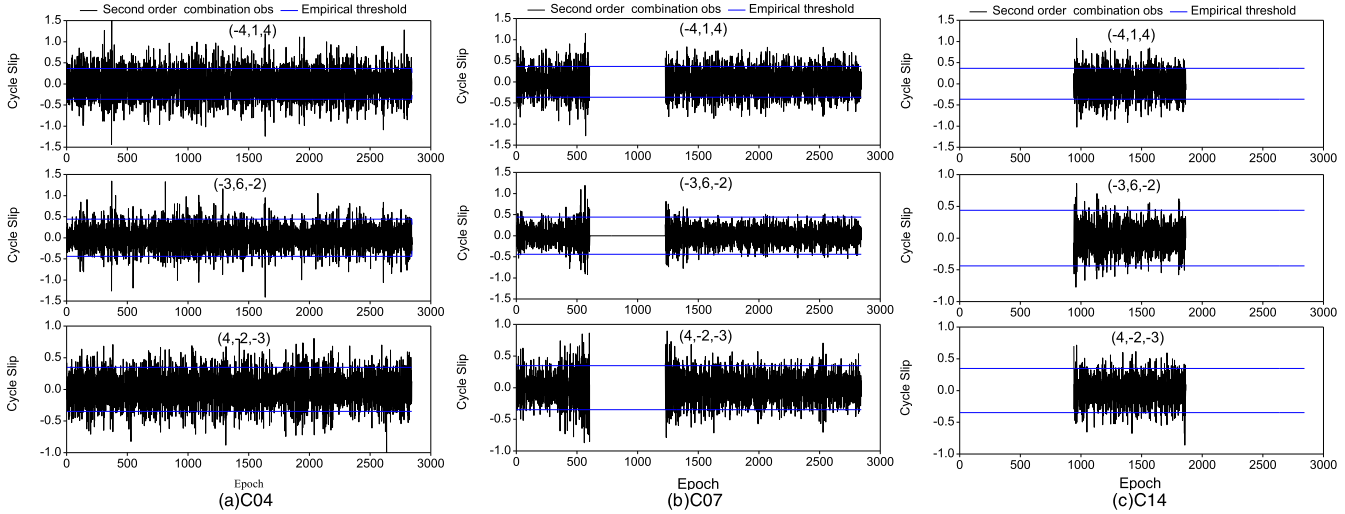

FIGURE 7. Second-order time-difference combination without cycle slips for observations with high noises for C04, C07, and C14 (Obs2).

TABLE 4. Cycle slip detection and repair results obtained with the ET method and AT method (static test).

PRN	Epoch of the cycle slip	Simulated Cycle Slip	$\Delta N_{\alpha_1\beta_1\gamma_1}$	$\Delta N_{\alpha_2\beta_2\gamma_2}$	$\Delta N_{\alpha_3\beta_3\gamma_3}$	Computed Integer Cycle Slip	
						ET	AT
C04	168	1,1,1	0.45	0.24	-0.42	Repair failed	1,1,1 (right)
	701	0, 1,0	-0.46	-5.45	1.41	1,0,1 (wrong)	0,-1,0 (right)
	718	4,3,3	-0.39	0.36	0.42	Repair failed	4,3,3 (right)
C07	523	1,1,1	0.16	-0.21	-0.10	Detect failed	1,1,1 (right)
	577	9,9,9	6.92	7.09	-7.02	7,7,7 (wrong)	9,9,9 (right)
	1288	3,3,2	-0.21	5.83	-0.79	4,4,3 (wrong)	3,3,2 (right)
C14	1013	4,3,3	-0.37	-0.47	0.40	Repair failed	4,3,3 (right)
	1051	1,1,1	1.41	1.36	-1.51	-25,-19,-20 (wrong)	1,1,1 (right)
	1843	0,0,1	3.44	-2.17	-2.62	-22,-17,-17 (wrong)	0,0,1 (right)

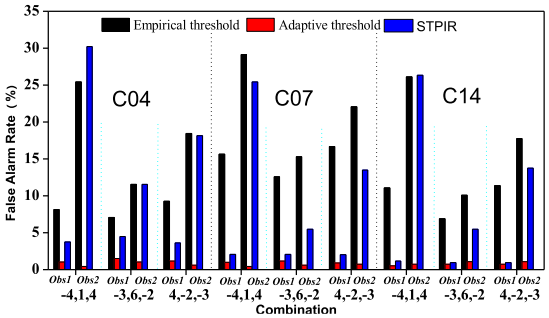

FIGURE 8. Statistics of false alarms of the empirical threshold, adaptive threshold and STPIR methods.

When the following condition is satisfied, a cycle slip can be detected.

$$\left|\nabla\Delta l_{\alpha\beta\gamma,abc}\right| > \kappa \cdot \sqrt{2}\sigma_{\Delta N_{\alpha\beta\gamma}} \tag{26}$$

Two sets of observations with different noise levels were simulated to investigate the performance of the STPIR method in detecting cycle slips. Figure 6 shows the second-order time-difference combination for the observations without cycle slips and with low noises (Obs1). Figure 7 shows the cycle slip detection results with the second-order time-difference combination for observations without cycle slips and with high noises (Obs2).

As shown in Figure 6, although the STPIR method is helpful for mitigating the impact of between-epoch ionospheric residuals, it also enlarges the pseudorange noise and leads to many false alarms in the low-elevation observations. For example, for the observations of the satellite C04, which are below the elevation of 30°, there are many false alarms obtained with the STPIR method. Moreover, it can be seen from Figure 7 that the STPIR method with the empirical

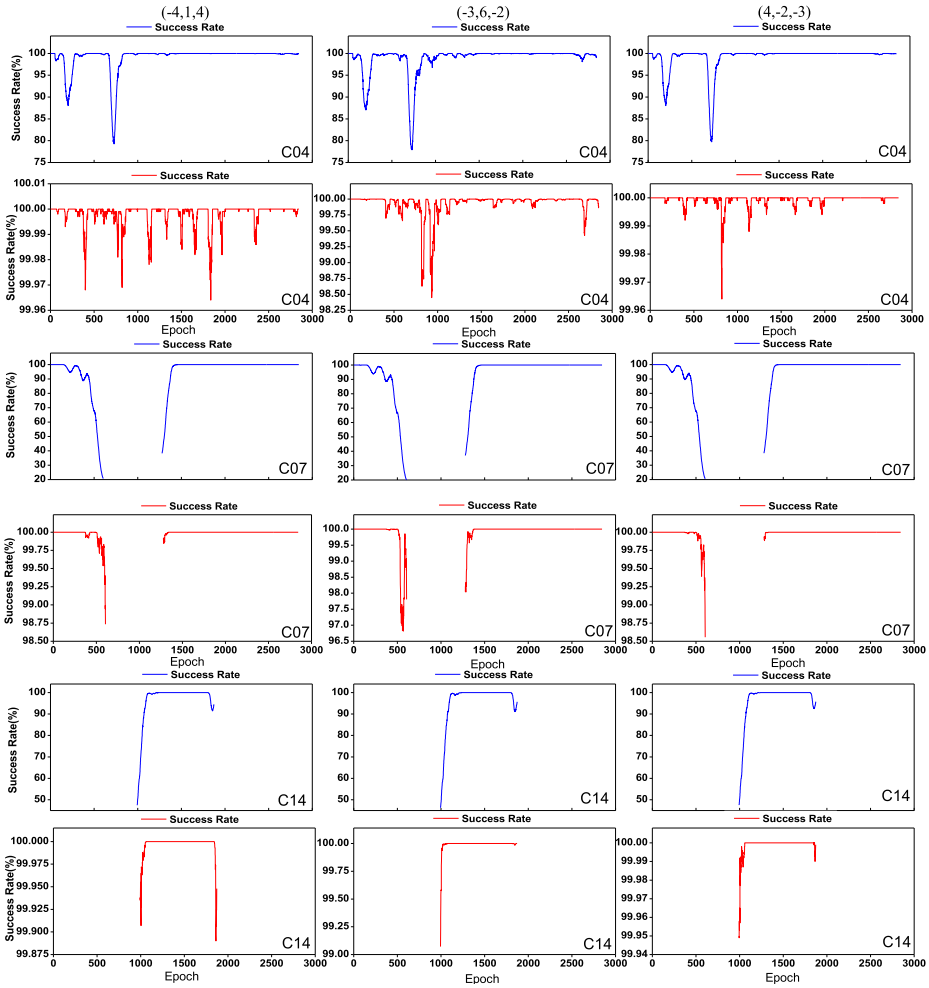

FIGURE 9. The rounding success rates of the ET method (blue) and the AT method (red) for static observations.

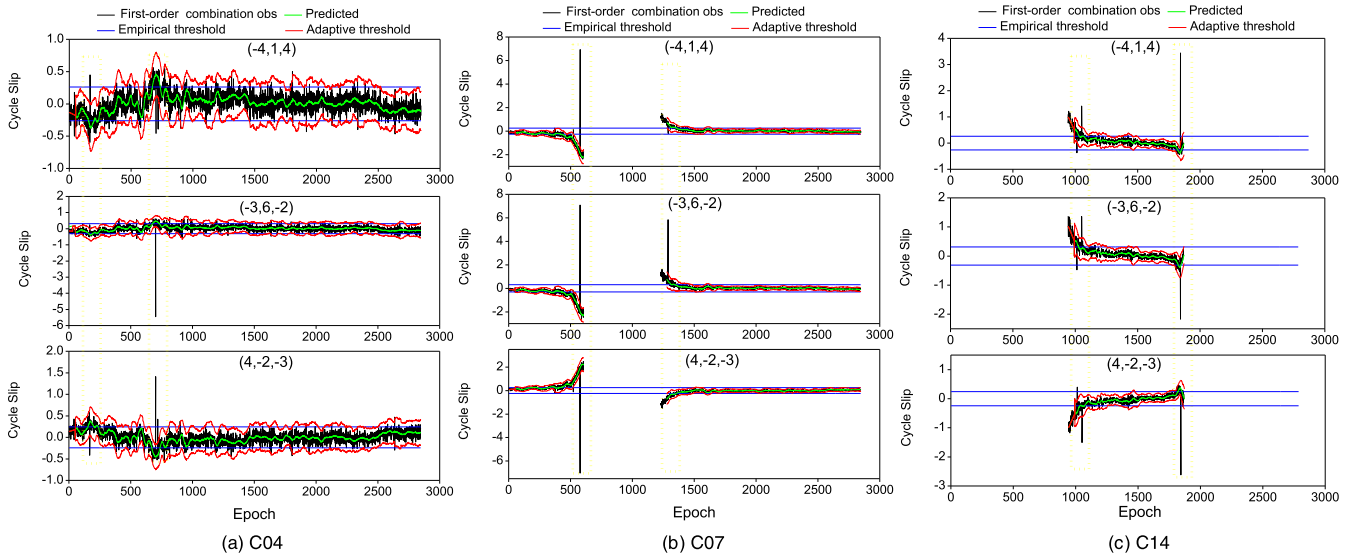

FIGURE 10. Cycle slip detection by the AT method with simulated cycle slips for C04, C07, and C14.

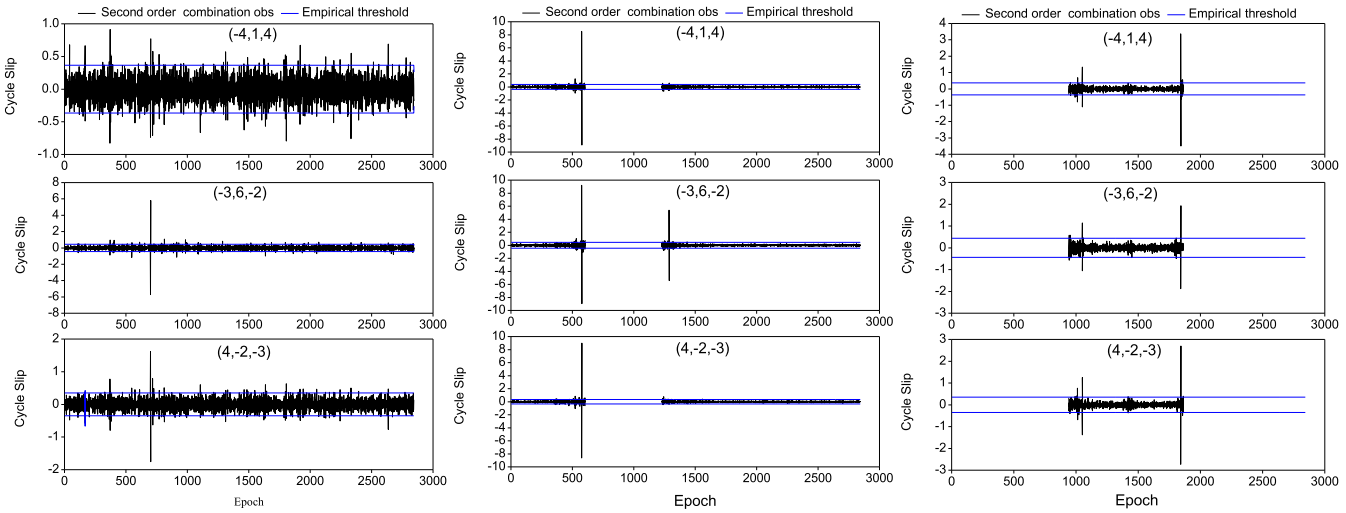

FIGURE 11. Cycle slip detection by the STPIR method with simulated cycle slips for C04, C07, and C14.

FIGURE 12. Trajectory of the car.

threshold will lead to many false alarms for observations with large pseudorange noise.

Some observations without cycle slip are removed by mistake due to the false alarms. It is necessary to reduce the false alarms. Table 3 shows a comparison of the false alarms obtained with three algorithms for Obs1 and Obs2. Figure 8 shows the false alarm rates of the three algorithms: the black bars are the false alarm rates of the empirical threshold method, the red bars are the false alarm rates of the adaptive threshold method, and the blue bars are the false alarm rates of the STPIR method.

The results show that the AT method proposed in this study can greatly reduce the number of false alarms in cycle slip detections for observations with high or low noise observations levels. For observations with a low noise level, both the AT method and STPIR method have better performances than the ET method. Compared to the ET method, the false alarm rate is reduced by 91% for the AT method and reduced by an average of 75% for the STPIR method. For observations with a high noise level, the AT method shows a much better performance than either the ET method or the STPIR method. For high-noise observations, the false alarm rate of the STPIR is only reduced by 18% on average, and the false alarm rate of the STPIR at some satellites (such as C04, with an elevation of 30°) is even larger than that of ET method. Therefore, the AT method has a lower false alarm rate than the STPIR method.

Figure 9 shows the direct rounding success rates of the ET method and the AT method in the case of the cycle slips of all epochs in the raw observations. From the comparison of the success rates, it can be seen that the AT method has a better performance than the ET method in determining the integer values of cycle slips. The rounding success rates of the ET method for satellite C04 are between 75% and 100%, while the rounding success rate of the AT method is increased to over 99.25%. The rounding success rates of the ET method for satellite C07 are between 20% and 100%, while the rounding success rate of the AT method is increased to over 96.50%. The rounding success rates of the ET method for satellite C14 are between 45% and 100%, while the rounding success rate of the AT method is increased to over 99.00%. The results shown in Figure 9 also indicate that the performance of the ET method decreases with lowered elevation, while the performance of the AT method does not show an obvious dependence on the elevation. Based on a large number of experiments, the success rate of the determination of the integer values of cycle slips can reach more than 95%.

The AT method was also validated by the data that were constructed by adding simulated cycle slips into the raw observations. The cycle slip simulation method and the detection results for these simulated observations are shown in Figure 10 and Table 4. It is easy to detect large cycle slips; therefore, several small cycle slips were simulated to investigate the performances of the AT method and the ET method in detecting small cycle slips.

It can be seen from Figures 9-10 and Table 4 that the direct rounding method fails to detect or repair simulated cycle slips. However, the AT method can not only reduce false alarms in the cycle slip detection but can also successfully detect and repair all simulated cycle slips.

To compare the performances of the STPIR method and the AT method in detecting cycle slips, the STPIR method was then applied to the same observations with simulated

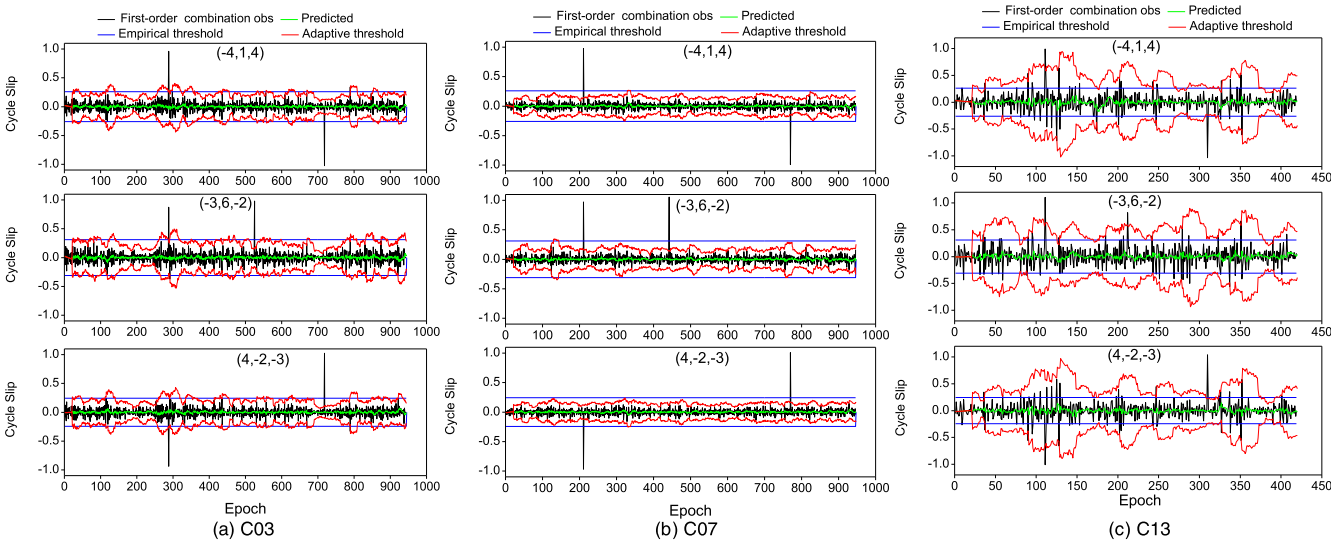

FIGURE 13. Cycle slip detection by the AT method with simulated cycle slips for C03, C07, and C13 with sampling intervals of 1 s.

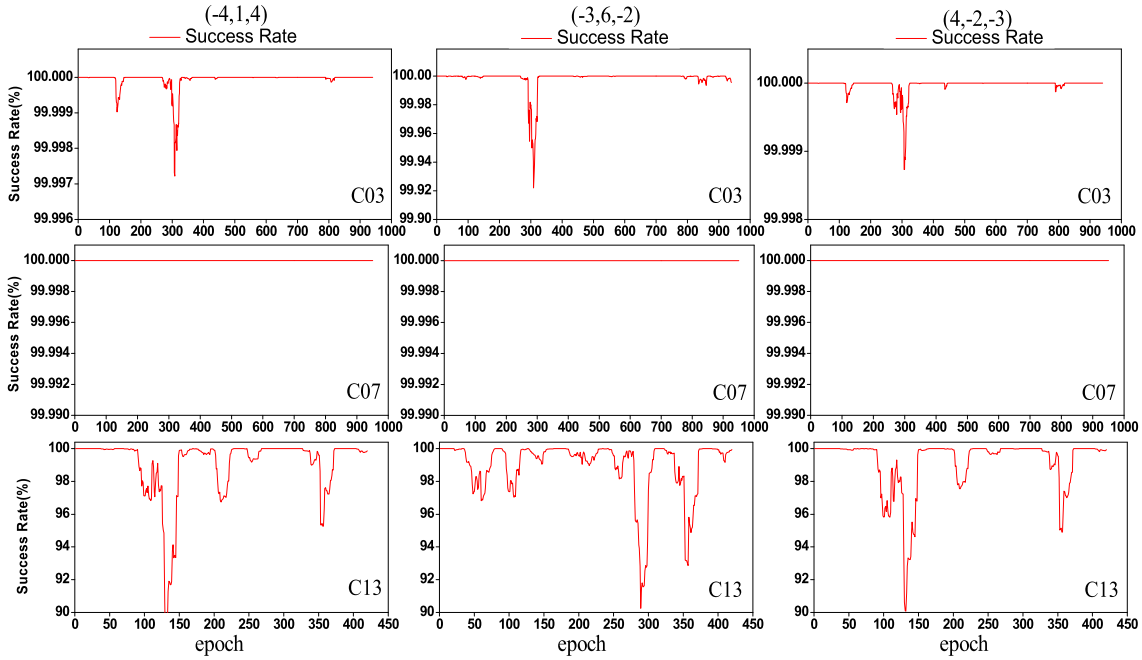

FIGURE 14. Rounding success rate of the AT method for the kinematic observations.

cycle slips. The simulated cycle slips and the detection results obtained with the STPIR method are shown in Table 5 and Figure 11.

According to [16], the combined-integer cycle slips were obtained by rounding the estimated combined cycle slips in columns 4-6 of Table 5. It can be seen from Figure 11 and Table 5 that 2 of the 9 simulated cycle slips failed to be detected with the STPIR method, and 338 (C04), 137 (C07) and 29 (C14) false alarms were reported in the cycle slip detection. When using the AT method, all simulated cycle slips were successfully detected and repaired, and only 105 (C04), 68 (C07) and 19 (C14) cycle slip false alarms were reported, as shown in Table 3.

As suggested by the previous results, the STPIR method may fail to detect small cycle slips. To further investigate the performances of two methods in detecting small cycle slips, a cycle slip (1,1,1) was added to the observations at each epoch, and these two methods were applied to these data to detect cycle slips. The results show that 66, 55, and 13 cycle slips were incorrectly repaired for C04, C07, and C14 with the STPIR method, respectively, while only 12, 15 and 12 cycle slips failed to be detected with the AT method proposed in this

TABLE 5. Cycle slip detection and repair results obtained with the STPIR method (static test).

PRN	Epoch of the cycle slip	Simulated Cycle Slip	$\Delta\nabla N_{\alpha_1\beta_1\gamma_1}$	$\Delta\nabla N_{\alpha_2\beta_2\gamma_2}$	$\Delta\nabla N_{\alpha_3\beta_3\gamma_3}$	Computed Integer Cycle Slip
C04	168	1,1,1	0.66	0.44	-0.67	-4,-3,-3 (wrong)
	701	0,-1,0	-0.74	-5.71	1.62	0,-1,0 (right)
	718	4,3,3	-0.70	0.04	0.79	4,3,3 (right)
C07	523	1,1,1	1.24	0.61	-1.05	1,1,1 (right)
	577	9,9,9	8.53	9.22	-8.64	9,9,9 (right)
	1288	3,3,2	-0.54	5.40	-0.41	3,3,2 (right)
C14	1013	4,3,3	-0.80	-0.33	0.76	4,3,3 (right)
	1051	1,1,1	1.33	1.14	-1.38	1,1,1 (right)
	1843	0,0,1	3.36	-1.87	-2.73	-22,-17,-17 (wrong)

TABLE 6. Cycle slip detection and repair results obtained with the AT method (kinematic test).

PRN	Epoch of the cycle slip	Simulated Cycle Slip	$\Delta N_{\alpha_1\beta_1\gamma_1}$	$\Delta N_{\alpha_2\beta_2\gamma_2}$	$\Delta N_{\alpha_3\beta_3\gamma_3}$	Computed Integer Cycle Slip
C03	288	1,1,1	0.962	0.874	-0.939	1,1,1(right)
	525	5,4,4	-0.025	0.981	0.024	5,4,4(right)
	718	4,3,3	-1.026	-0.020	1.024	4,3,3(right)
C07	211	1,1,1	0.978	0.975	-0.971	1,1,1(right)
	442	5,4,4	-0.020	1.055	0.018	5,4,4(right)
	770	4,3,3	-0.993	-0.053	1.007	4,3,3(right)
C13	111	1,1,1	0.993	1.104	-1.009	1,1,1(right)
	212	5,4,4	-0.013	0.820	0.043	5,4,4(right)
	310	4,3,3	-0.035	-0.092	1.039	4,3,3(right)

study, respectively. Moreover, the experiments also indicated that the AT method can detect and repair cycle slips more accurately than the STPIR method for observations with a high noise level. Therefore, the comparison of the results of the two methods indicates that the performance of the AT method is better than that of STPIR method, especially for observations with a high noise level.

B. EXPERIMENT WITH KINEMATIC OBSERVATIONS

To further investigate the performance of the AT method in detecting and repairing cycle slips, an experiment was conducted by applying this method to dynamic data collected with a vehicle-based receiver. The BDS kinematic data were collected in Tai' an, China, on Jun. 1, 2020 with a time period of 16 minutes and a mean speed of approximately 40 km/hour. It should be noted that the ionosphere was quiet during this experiment. The sampling interval was 1s, and the GNSS receiver used in the test was a South Yinhe1 receiver. The trajectory of the car is shown in Figure 12. As shown in Table 6, nine cycle slips were simulated and added to these observations. Figures 13-14 and Table 6 provide the cycle-slip detection and repair results obtained with the AT method.

It is apparent in Figures 13-14 and Table 6 that the AT method also has a very good performance in effectively

detecting and repairing cycle slips in the kinematic observations that are as small as one cycle, even though the pseudorange noise observed during the kinematic experiments was generally large. Compared to the AT method, the false alarm rate of the ET method in detecting cycle slips was relatively high. The success rate of rounding based on the ionospheric delay prediction model was over 99.92% for C03 and C07. Because of the high pseudorange noise of the C13 observations, the success rate of rounding with the AT method was slightly lower but was still over 90%.

VI. CONCLUSION

In this paper, a real-time cycle slip detection and repair method was proposed for BDS that is not limited by an active ionospheric condition. Using three linearly independent GF pseudorange minus phase combinations, most cycle slips can be detected and repaired reliably in benign situations. However, in cases of low elevations and/or under active ionospheric conditions, successful cycle slip detections and repairs become challenging. The newly proposed method constructs an adaptive threshold by combining predicted epoch-differenced ionospheric delays to improve the cycle slip detection performance, and a new rounding method considering the predicted epoch-differenced ionospheric delays is proposed to obtain a higher success rate for estimating the integer values of cycle slips.

This approach has many advantages. First, the AT method can detect all small cycle slips including insensitive cycle slips. Second, even if the ionospheric delay changes rapidly, the AT method reduces the false alarm rate of the cycle slip detection by predicting the epoch-difference of the ionospheric delay. Finally, the predicted epoch-differenced ionospheric delay is considered before the estimations are rounded; thus, the rounding success rate is increased. Compared with the time-consuming theoretically optimal method, this newly proposed method is more efficient for determining the integer values of cycle slips, which is very important for many real-time applications. Therefore, this method can achieve efficient cycle slip detections and real-time repairs.

The validity of this method is verified by static and dynamic data. The results show that the false alarm rate is reduced by 91% with the AT method and this method can accurately detect and repair cycle slips as small as one cycle even if the ionosphere is active. However, the performance of this method may be affected by the pseudorange noise level. When the pseudorange noise is very high, although this method can reduce the false alarm rate, the cycle slip detection performance is also reduced. Thus, this feature of the proposed method should be studied, and the AT method should be used together with other methods.

REFERENCES

[1] S. Han, Z. Gong, W. Meng, C. Li, and W. Tang, "Automatic precision control positioning for wireless sensor networks," *IEEE Sensors J.*, vol. 16, no. 7, pp. 2140–2150, Apr. 2016.
[2] L. Yin, S. Li, Z. Deng, and D. Zhu, "A novel cycle slips detection model for the high precision positioning," *IEEE Access*, vol. 7, pp. 24041–24050, Jan. 2019.
[3] Y. G. Z. Li, "Cycle slip detection and ambiguity resolution algorithms for dual-frequency GPS data processing," *Mar. Geodesy*, vol. 22, no. 3, pp. 169–181, Jul. 1999.
[4] S. B. Bisnath and R. B. Langley, "Efficient, automated cycle-slip correction of dual-frequency kinematic GPS data," in *Proc. 13th Int. Tech. Meeting Satell. Division Inst. Navigat. (ION GPS)*, 2000, pp. 145–154.
[5] D. Chen, S. Ye, W. Zhou, Y. Liu, P. Jiang, W. Tang, B. Yuan, and L. Zhao, "A double-differenced cycle slip detection and repair method for GNSS CORS network," *GPS Solutions*, vol. 20, no. 3, pp. 439–450, Jul. 2016.
[6] G. Blewitt, "An automatic editing algorithm for GPS data," *Geophys. Res. Lett.*, vol. 17, no. 3, pp. 199–202, Mar. 1990.
[7] B. Ju, D. Gu, X. Chang, T. A. Herring, X. Duan, and Z. Wang, "Enhanced cycle slip detection method for dual-frequency BeiDou GEO carrier phase observations," *GPS Solutions*, vol. 21, no. 3, pp. 1227–1238, Jul. 2017.
[8] B. Li, Y. Qin, and T. Liu, "Geometry-based cycle slip and data gap repair for multi-GNSS and multi-frequency observations," *J. Geodesy*, vol. 93, no. 3, pp. 399–417, Mar. 2019.
[9] Z. Liu, "A new automated cycle slip detection and repair method for a single dual-frequency GPS receiver," *J. Geodesy*, vol. 85, no. 3, pp. 171–183, Mar. 2011.
[10] X. Gu and B. Zhu, "An improved ambiguity resolution of three carriers in precise point positioning," *IEEE Access*, vol. 6, pp. 3951–3961, Jan. 2018.
[11] H. Qin, P. Liu, J. Qu, and L. Cong, "Optimal carrier-phase integer combinations for modernized triple-frequency BDS in precise point positioning," *IEEE Access*, vol. 7, pp. 177449–177459, Dec. 2019.
[12] Z. Dai, S. Knedlik, and O. Loffeld, "Real-time cycle-slip detection and determination for multiple frequency GNSS," in *Proc. 5th Workshop Positioning, Navigat. Commun.*, Hannover, Germany, Mar. 2008, pp. 37–43.
[13] M. C. de Lacy, M. Reguzzoni, and F. Sansò, "Real-time cycle slip detection in triple-frequency GNSS," *GPS Solutions*, vol. 16, no. 3, pp. 353–362, Jul. 2012.
[14] S. Banville and R. B. Langley, "Mitigating the impact of ionospheric cycle slips in GNSS observations," *J. Geodesy*, vol. 87, no. 2, pp. 179–193, Feb. 2013.
[15] C. Cai, Z. Liu, P. Xia, and W. Dai, "Cycle slip detection and repair for undifferenced GPS observations under high ionospheric activity," *GPS Solutions*, vol. 17, no. 2, pp. 247–260, Apr. 2013.
[16] W. Liu, X. Jin, M. Wu, J. Hu, and Y. Wu, "A new real-time cycle slip detection and repair method under high ionospheric activity for a triplefrequency GPS/BDS receiver," *Sensors*, vol. 18, no. 2, pp. 427–448, 2018.
[17] L. Huang, G. Zhai, Y. Ou, X. Lu, T. Wu, and K. Deng, "Triple-frequency TurboEdit cycle-slip processing method of weakening ionospheric activity," *Acta Geodaetica et Cartographica Sinica*, vol. 44, no. 8, pp. 840–847, 2015.
[18] A. Renga, F. Causa, U. Tancredi, and M. Grassi, "Accurate ionospheric delay model for real-time GPS-based positioning of LEO satellites using horizontal VTEC gradient estimation," *GPS Solutions*, vol. 22, no. 2, p. 46, Feb. 2018.
[19] X. Gu and B. Zhu, "Detection and correction of cycle slip in triple-frequency GNSS positioning," *IEEE Access*, vol. 5, pp. 12584–12595, Jun. 2017.
[20] G. Chang, T. Xu, Y. Yao, H. Wang, and H. Zeng, "Ionospheric delay prediction based on online polynomial modeling for real-time cycle slip repair of undifferenced triple-frequency GNSS signals," *Measurement*, vol. 146, pp. 289–297, Nov. 2019.
[21] Q. Zhao, B. Sun, Z. Dai, Z. Hu, C. Shi, and J. Liu, "Real-time detection and repair of cycle slips in triple-frequency GNSS measurements," *GPS Solutions*, vol. 19, no. 3, pp. 381–391, Jul. 2015.
[22] G. Chang, T. Xu, Y. Yao, and Q. Wang, "Adaptive Kalman filter based on variance component estimation for the prediction of ionospheric delay in aiding the cycle slip repair of GNSS triple-frequency signals," *J. Geodesy*, vol. 92, no. 11, pp. 1241–1253, Nov. 2018.
[23] C. Deng, J. Cui, W. Tang, X. Zou, and L. Shu, "Reliable real-time triple-frequency cycle slip detection and recovery with adaptive detection thresholds," *Meas. Sci. Technol.*, vol. 30, no. 5, pp. 348–365, Apr. 2019.
[24] T. Richert and N. El-Sheimy, "Optimal linear combinations of triple frequency carrier phase data from future global navigation satellite systems," *GPS Solutions*, vol. 11, no. 1, pp. 11–19, Mar. 2006.
[25] S. Han and C. Rizos, "The impact of two additional civilian GPS frequencies on ambiguity resolution strategies," in *Proc. 55th Annu. Meeting Inst. Navigat. (ION GPS)*, 1999, pp. 315–321.
[26] P. J. G. Teunissen, "Success probability of integer GPS ambiguity rounding and bootstrapping," *J. Geodesy*, vol. 72, no. 10, pp. 606–612, Oct. 1998.

[27] Y. Feng, "GNSS three carrier ambiguity resolution using ionosphere-reduced virtual signals," *J. Geodesy*, vol. 82, no. 12, pp. 847–862, Feb. 2008.
[28] C. Zhang, Q. Xu, and Z. Li, "Improving method of cycle slip detection and correction based on combination of GPS pseudo range and carrier phase observations," *Acta Geodaetica et Cartographica Sinica*, vol. 38, no. 5, pp. 402–407, May 2009.
[29] B. Li, Y. Qin, Z. Li, and L. Lou, "Undifferenced cycle slip estimation of triple-frequency BeiDou signals with ionosphere prediction," *Mar. Geodesy*, vol. 39, no. 5, pp. 348–365, Sep. 2016.
[30] B. Li, T. Liu, L. Nie, and Y. Qin, "Single-frequency GNSS cycle slip estimation with positional polynomial constraint," *J. Geodesy*, vol. 93, no. 9, pp. 1781–1803, Jul. 2019.
[31] P. J. G. Teunissen, "Integer estimation in the presence of biases," *J. Geodesy*, vol. 75, nos. 7–8, pp. 399–407, Sep. 2001.

CHENXI ZHANG received the Ph.D. degree in geodesy and survey engineering from the Shandong University of Science and Technology, in 2018. Her current research interests include multi-frequency GNSS data processing and stochastic modeling.

YAMIN DANG received the Ph.D. degree in geodesy from Wuhan University, Wuhan, China, in 1999. He is currently a Professor of Geodesy and the Director of the Institute of Geodesy and Geodynamics with the Chinese Academy of Surveying and Mapping. His research interests include GNSS data processing, regional crustal deformation analysis and modeling by using space geodetic techniques, tectonic plate motion and geodynamics, geodetic datum, and reference frames.

XIAOMING WANG received the Ph.D. degree in global navigation satellite system (GNSS) meteorology from RMIT University, Melbourne, VIC, Australia, in 2017. He is currently an Associate Professor with the Aerospace Information Research Institute, Chinese Academy of Sciences, Beijing, China. His research interests include GNSS precise positioning and GNSS meteorology.

JINYI QUAN received the M.S. degree from the Shandong University of Science and Technology, in 2005. His current research interests include multi-system algorithms of precise point positioning and cooperative positioning.

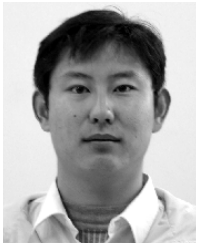

ZHIGANG YU received the M.S. degree from the Shandong University of Science and Technology, Qingdao, China, in 2006, where he is currently pursuing the Ph.D. degree with the School of Geodesy and Geomatics. His current research interests include high accuracy positioning and InSAR technology.